Open Access

Journal of Energy and Power Technology

LIDSEN Publishing Inc.

Original Research

A Novel Approach to Carbon Monoxide Removal Using Transition Metal-Doped Boron Nitride Nanosensors for Environmental Sustainability

Fatemeh Mollaamin *

Department of Biomedical Engineering, Faculty of Engineering and Architecture, Kastamonu University, Kastamonu, Turkey; E-Mail: fmollaamin@kastamonu.edu.tr

* **Correspondence:** Fatemeh Mollaamin; E-Mail: fmollaamin@kastamonu.edu.tr

Academic Editor: Junkuo Gao

Journal of Energy and Power Technology
2025, volume 7, issue 2
doi:10.21926/jept.2502006

Received: November 12, 2024
Accepted: March 27, 2025
Published: April 02, 2025

Abstract

Adsorption of toxic gas of CO molecules by using transition metals of X (X = Ti, V, Cr, Co, Cu, Zn)-doped boron nitride nanocage (B_5N_{10}_NC) has been studied by computational chemistry. Based on NQR analysis, X-doped on B_5N_{10}_NC has shown the lowest fluctuation in electric potential and the highest negative atomic charge, including 0.2331 (copper), 0.3112 (cobalt), 0.5883 (chromium), 0.6853 (zinc), 0.6893 (vanadium) and 0.7499 coulomb (titanium), respectively, have presented the most tendency for being the electron acceptors. Moreover, the parameters of the NMR method have indicated that the yield of electron-accepting for doping atoms on the X–B_4N_{10}_NC through gas molecules adsorption can be ordered as Cu > Co >> Cr > Zn ≈ V > Ti that exhibits the strength of the covalent bond between titanium, vanadium, chromium, cobalt, copper, zinc, and CO towards toxic gas removal from air. The adsorption of CO gas molecules can remark spin polarization on the X–B_4N_{10}_NC, which specifies that these nano-surfaces may be employed as magnetic scavenging surfaces as a gas detector. Regarding IR spectroscopy, doped nanocages of Ti–B_4N_{10}_NC, V–B_4N_{10}_NC, Cr–B_4N_{10}_NC, Co–B_4N_{10}_NC, Cu–B_4N_{10}_NC and Zn–B_4N_{10}_NC, respectively, have the most fluctuations and the highest adsorption tendency for gas molecules which can direct specific inquiries on the individual impact of charge carriers (gas molecule-nanocage), as well as doping atoms on the overall structure. The Gibbs free energy has shown that the maximum efficiency of Ti, V, Cr, Co, Cu, and Zn atoms doping of B_5N_{10}_NC for gas molecules adsorption

depends on the covalent bond between CO molecules and X–B_4N_{10}_NC as a potent sensor for air pollution removal. Therefore, for a given number of carbon donor sites in CO, the stabilities of complexes owing to doping atoms of Ti, V, Cr, Co, Cu, Zn can be taken into account as: CO@Cu–B_4N_{10}_NC >> CO@Co–B_4N_{10}_NC > CO@Cr–B_4N_{10}_NC > CO@V–B_4N_{10}_NC > CO@Zn–B_4N_{10}_NC > CO@Ti–B_4N_{10}_NC.

Keywords
CO removal; gas detecting; nanomaterials; transition metals; DFT

1. Introduction

The privileged attributes of boron nitrides, mainly structural and electronic, have made them proper for pollutant adsorption and semiconducting properties [1-4]. Boron nitride nanomaterials usually exhibit semi-leading behavior, which is considered an appropriate alternative to carbon nanotubes. The unique properties of boron and nitrogen atoms make boron nitride an interesting subject of numerous studies [5-7].

In recent years, different investigations on the adsorption of chemical contaminants and applying various boron nitride nanostructures as adsorbents for water purification have been studied [8-10].

Various physical shapes of boron nitride (BN)-based nano adsorbents such as nanoparticles, fullerenes, nanotubes, nanofibers, nanoribbons, nanosheets, nanomeshes, nanoflowers, and hollow spheres have been broadly considered possible adsorbents owing to their exceptional characteristics such as large surface area, structural variability, great chemical/mechanical strength, abundant structural defects, high reactive sites, and functional groups [11, 12].

Carbon monoxide (CO), carbon dioxide and methane are environmental problems. CO is a toxic gas that, at standard conditions, is tasteless, odorless, and colorless. It comes primarily from incomplete combustion of carbon-containing fuels. It is not irritating, and it is an asphyxiant. At high levels, it is deadly. The investigation of the adsorption of carbon monoxide on palladium and transition metals is an attractive research topic [13].

The researchers have applied Density functional theory for the computation of geometry optimizations, binding and adsorption energies, and electronic properties of CO molecule adsorption on pristine and group 8B transition metal (TM)–doped boron nitride nanosheets (BNNS). They exhibited that the TM atom displays strong binding with B and N vacancy BNNSs with energy gaps of TM–doped BNNS smaller than that of pristine BNNS. The CO tends to attach via its C and O atoms to TM–doped BNNSs with more considerable adsorption energy and smaller adsorption distance than that of pristine BNNS [14].

The interactions between carbon monoxide gas and boron nitride nanocage were investigated using two DFT functionals (B3LYP and B97D) and a 6-31G(d) basis set. The computational results indicated the capability of $B_{12}N_{12}$ as a sensor for potential applications in the detection of CO under an external electric field [15, 16].

2. Materials and Methods

This research article wants to remove toxic gas molecules, including CO, from the air through an eco-friendly approach by using (Ti, V, Cr, Co, Cu, Zn)-doped B_5N_{10}_NC (Figure 1).

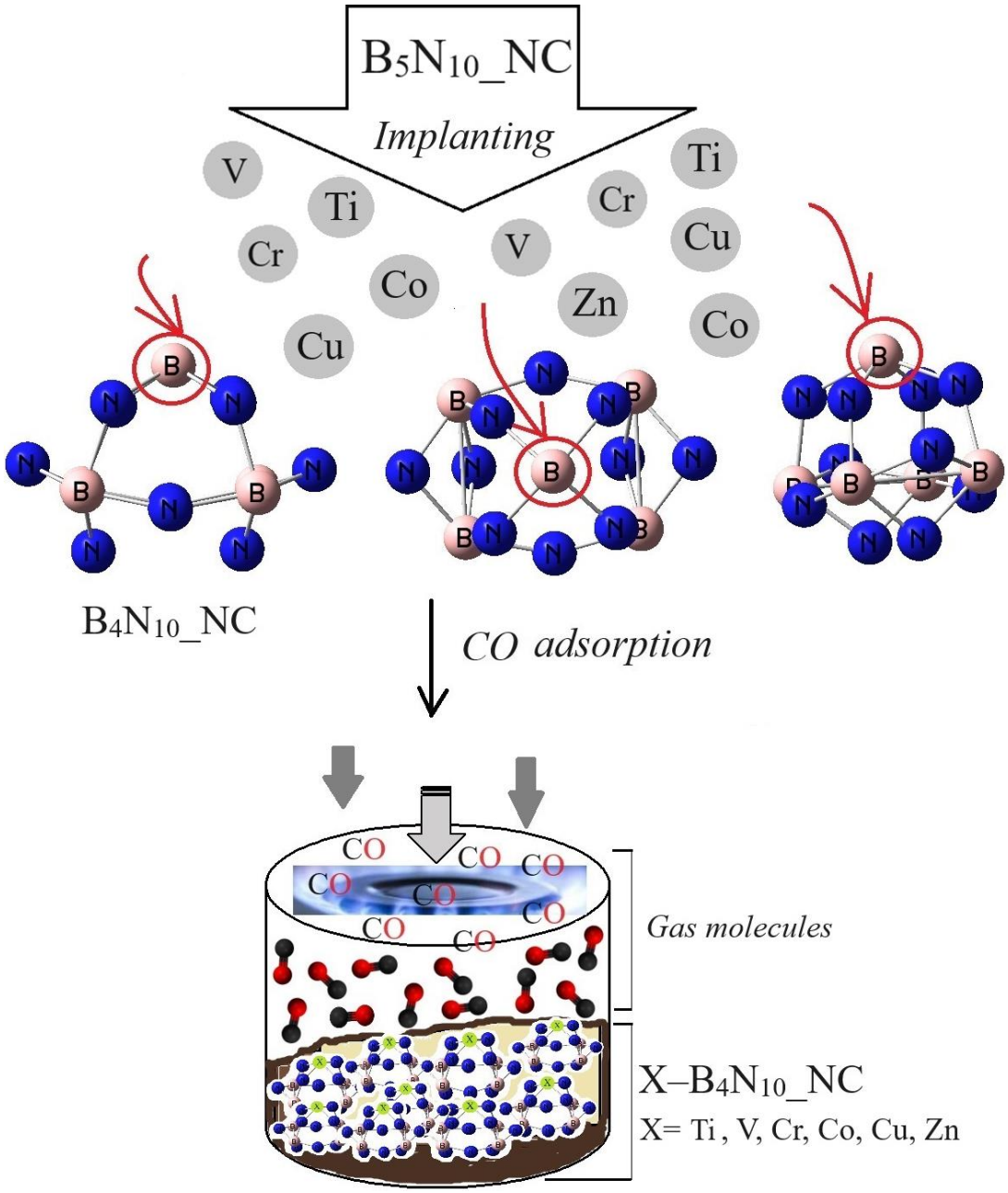

Figure 1 Application of X–B_4N_{10}_NC towards adsorption of gas molecules of CO and formation of complexes: "CO@Ti–B_4N_{10}_NC, CO@V–B_4N_{10}_NC, CO@Cr–B_4N_{10}_NC, CO@Co–B_4N_{10}_NC, CO@Cu–B_4N_{10}_NC, CO@Zn–B_4N_{10}_NC" complexes.

Boron nitride nanocage has been designed owing to doping atoms of titanium, vanadium, chromium, cobalt, copper, and zinc which can increase the gas sensing potential of BN-nanocage.

Figure 1 has declared the status of CO adsorption on the X–B_4N_{10}_NC surface which towards formation of complexes containing CO@Ti–B_4N_{10}_NC, CO@V–B_4N_{10}_NC, CO@Cr–B_4N_{10}_NC, CO@Co–B_4N_{10}_NC, CO@Cu–B_4N_{10}_NC, CO@Zn–B_4N_{10}_NC by computational chemistry.

The charge distribution of the mentioned complexes is calculated due to the Bader charge analysis [17]. The trapping of CO molecules by X–B_4N_{10}_NC (X = Ti, V, Cr, Co, Cu, Zn) was successfully incorporated due to binding formation consisting of C → Ti, C → V, C → Cr, C → Co, C → Cu, C → Zn (Figure 1).

Development of the applied Density Functional Theory (DFT) methodology only became notable after W. Kohn and L. J. Sham released their reputable series of equations which are introduced as Kohn-Sham (KS) equations [18-23]. So, one starts with a reference model of *M* with non-interacting electrons related to the external potential v_s and with Hamiltonian [24-31]:

$$\hat{H}_s = -\sum_i^M \frac{1}{2}\overline{\nabla}_i^2 + \sum_i^M v_s(\vec{r}_i) = \sum_i^M \hat{h}_s\,; \quad \hat{h}_s = -\frac{1}{2}\overline{\nabla}_i^2 + v_s(\vec{r}_i) \tag{1}$$

By representing the single particle orbitals ψ_i all electronic densities physically acceptable for the system of "non-interacting" electrons are written in the equation (2):

$$\rho(\vec{r}) = \sum_i^M |\psi_i(\vec{r})|^2 \tag{2}$$

Finally, the total energy could be measured by the KS method due to the equation (3):

$$E[\rho] = \sum_i^M n_i \left\langle \psi_i \left| -\frac{1}{2}\overline{\nabla}^2 + v_{ext}(\vec{r}) + \frac{1}{2}\int \frac{\rho(\vec{r}')}{|\vec{r}-\vec{r}'|}\mathrm{d}\vec{r}' \right| \psi_i \right\rangle + E_{xc}[\rho] + \frac{1}{2}\sum_\beta^N \sum_{\alpha\neq\beta}^N \frac{Z_\alpha Z_\beta}{|\vec{R}_\alpha - \vec{R}_\beta|} \tag{3}$$

In this article, the rigid PES using DFT calculations has been computed applying Gaussian 16 revision C.01 software [32]. The input Z-matrix for adsorption of CO molecules in air by the X–B_4N_{10}_NC has been designed with GaussView 6.1 [33] using 6–311+G (d,p), EPR–3, LANL2DZ basis set.

3. Results and Discussion

Electric field gradient (EFG) at the citation of the nucleus in CO is allocated by the valence electrons twisted in the attachment with close nuclei of X–B_4N_{10}_NC (X = Ti, V, Cr, Co, Cu, Zn) (Figure 2). So, "the nuclear quadrupole resonance (NQR) frequency" can be measured for CO@X–B_4N_{10}_NC complexes using Gaussian 16 revision C.01 software [32] (Table 1 & Table 2).

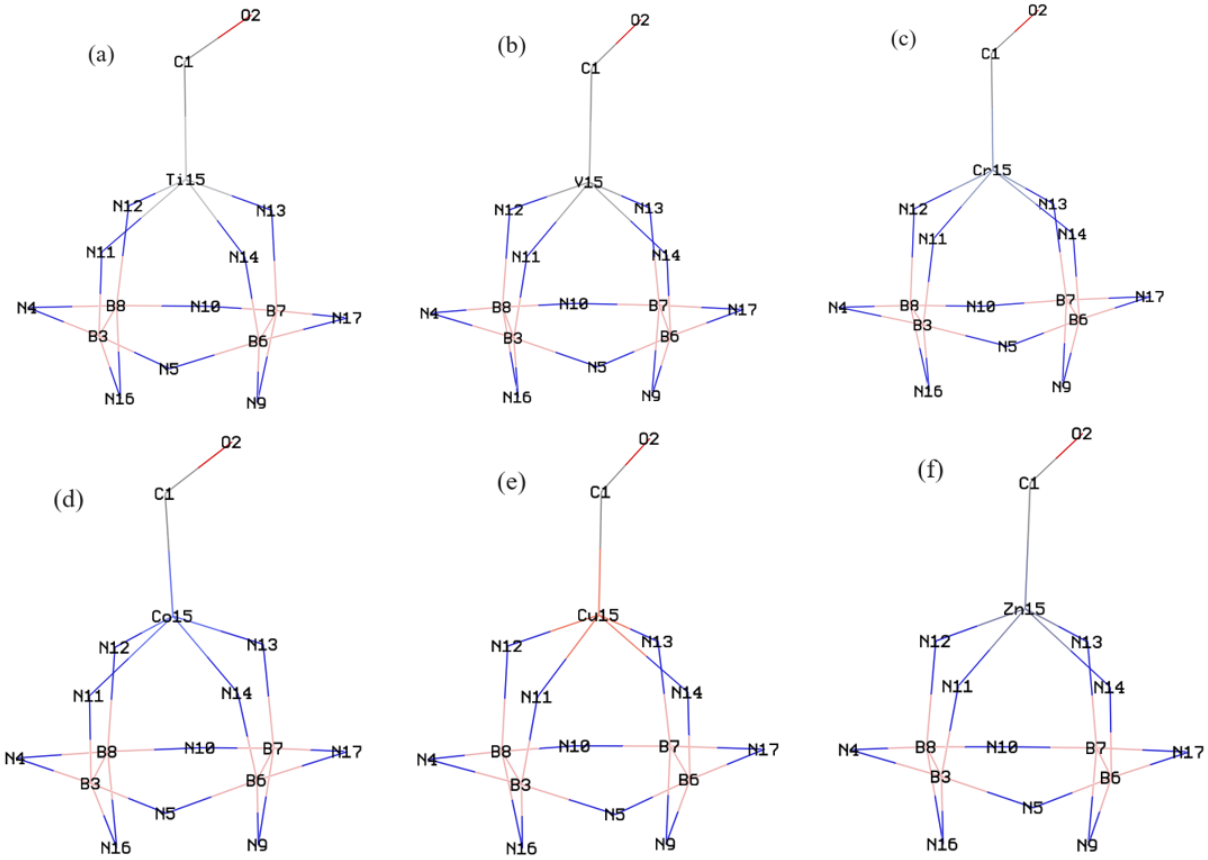

Figure 2 Carbon monoxide adsorbed on the surface of X–B_4N_{10}_NC (X = Ti, V, Cr, Co, Cu, Zn) towards the formation of **a)** CO@Ti–B_4N_{10}_NC, **b)** CO@V–B_4N_{10}_NC, **c)** CO@Cr–B_4N_{10}_NC, **d)** CO@Co–B_4N_{10}_NC, e**)** CO@Cu–B_4N_{10}_NC and **f)** CO@Zn–B_4N_{10}_NC.

Table 1 The electric potential (a.u.) and Bader charge (e) through NQR calculation for CO@Ti–B_4N_{10}_NC, CO@V–B_4N_{10}_NC, CO@Cr–B_4N_{10}_NC complexes.

CO@Ti–B_4N_{10}_NC			CO@V–B_4N_{10}_NC			CO@Cr–B_4N_{10}_NC		
Atom	Q	E_p	Atom	Q	E_p	Atom	Q	E_p
C1	0.1679	-14.5375	C1	0.0671	-14.5865	C1	0.1019	-14.5703
O2	-0.1297	-22.1646	O2	-0.1799	-22.2083	O2	-0.2053	-22.2094
B3	0.1532	-11.2825	B3	0.1170	-11.2803	B3	0.1285	-11.271
N4	-0.0479	-18.2904	N4	-0.0334	-18.2771	N4	-0.0515	-18.2755
N5	-0.0562	-18.2724	N5	-0.0760	-18.28	N5	-0.0936	-18.2746
B6	0.1410	-11.2804	B6	0.1205	-11.2795	B6	0.1442	-11.2733
B7	0.1480	-11.2816	B7	0.1114	-11.28	B7	0.1227	-11.2688
B8	0.1419	-11.2804	B8	0.1162	-11.2789	B8	0.1439	-11.2743
N9	-0.0585	-18.2696	N9	-0.0357	-18.2707	N9	-0.0452	-18.2605
N10	-0.0530	-18.2715	N10	-0.0718	-18.2783	N10	-0.0936	-18.2754
N11	-0.2665	-18.2967	N11	-0.1883	-18.2792	N11	-0.1418	-18.2607
N12	-0.2622	-18.2899	N12	-0.1888	-18.2783	N12	-0.1738	-18.2605
N13	-0.2641	-18.297	N13	-0.1862	-18.2803	N13	-0.1517	-18.2623
N14	-0.2600	-18.2899	N14	-0.1924	-18.279	N14	-0.1728	-18.2598
Ti15	0.7499	-10.8373	**V15**	0.6893	-12.535	**Cr15**	0.5883	-14.3983
N16	-0.0615	-18.2726	N16	-0.0362	-18.2701	N16	-0.0518	-18.2647
N17	-0.0423	-18.2889	N17	-0.0330	-18.2773	N17	-0.0483	-18.2739

Table 2 The electric potential (a.u.) and Bader charge (e) through NQR calculation for CO@Co–B_4N_{10}_NC, CO@Cu–B_4N_{10}_NC, and CO@Zn–B_4N_{10}_NC complexes.

CO@Co–B_4N_{10}_NC			CO@Cu–B_4N_{10}_NC			CO@Zn–B_4N_{10}_NC		
Atom	Q	E_p	Atom	Q	E_p	Atom	Q	E_p
C1	0.1255	-14.5643	C1	0.1820	-14.5522	C1	0.2162	-14.5178
O2	-0.1857	-22.2102	O2	-0.1756	-22.2044	O2	-0.1318	-22.1584
B3	0.1396	-11.2851	B3	0.1277	-11.2865	B3	0.0982	-11.2942
N4	-0.0346	-18.2779	N4	-0.0300	-18.2904	N4	-0.0316	-18.2923
N5	-0.0651	-18.2712	N5	-0.0630	-18.266	N5	-0.0690	-18.2603
B6	0.1314	-11.2867	B6	0.1262	-11.284	B6	0.1036	-11.2942
B7	0.1274	-11.2867	B7	0.1261	-11.2843	B7	0.0992	-11.2939
B8	0.1310	-11.284	B8	0.1203	-11.2865	B8	0.1032	-11.294
N9	-0.0676	-18.2828	N9	-0.0670	-18.2879	N9	-0.0513	-18.2827
N10	-0.0656	-18.2731	N10	-0.0635	-18.2662	N10	-0.0679	-18.2598
N11	-0.1153	-18.275	N11	-0.1046	-18.2728	N11	-0.2191	-18.2894
N12	-0.1171	-18.2739	N12	-0.1140	-18.272	N12	-0.2207	-18.2896
N13	-0.1067	-18.2718	N13	-0.0960	-18.2696	N13	-0.2109	-18.2884
N14	-0.1152	-18.2705	N14	-0.1140	-18.2688	N14	-0.2225	-18.2899
Co15	0.3112	-21.031	**Cu15**	0.2331	-26.0904	**Zn15**	0.6853	-16.151
N16	-0.0580	-18.2849	N16	-0.0597	-18.2861	N16	-0.0504	-18.2829
N17	-0.0350	-18.2876	N17	-0.0280	-18.288	N17	-0.0304	-18.292

The NQR method is related to the multipole expansion in Cartesian coordinates as the equation (4) [34, 35]:

$$V(r) = V(0) + \left[\left(\frac{\partial V}{\partial x_i}\right)\Big|_0 . x_i\right] + \frac{1}{2}\left[\left(\frac{\partial^2 V}{\partial x_i x_j}\right)\Big|_0 . x_i x_j\right] + \cdots \quad (4)$$

After that, a simplification on the equation (4), there are only the second derivatives related to the identical variable for the potential energy [34, 35]:

$$U = -\frac{1}{2}\int_{\mathcal{D}} d^3 r \rho_r \left[\left(\frac{\partial^2 V}{\partial x_i^2}\right)\Big|_0 . x_i^2\right] = -\frac{1}{2}\int_{\mathcal{D}} d^3 r \rho_r \left[\left(\frac{\partial E_i}{\partial x_i}\right)\Big|_0 . x_i^2\right] = -\frac{1}{2}\left(\frac{\partial E_i}{\partial x_i}\right)\Big|_0 . \int_{\mathcal{D}} d^3 r [\rho(r) . x_i^2] \quad (5)$$

There are two parameters which must be gotten from NQR experiments: the quadrupole coupling constant, χ, and asymmetry parameter of the EFG tensor η:

$$\chi = \frac{e^2 Q q_{zz}}{h} \quad (6)$$

$$\eta = \frac{q_{xx} - q_{yy}}{q_{zz}} \quad (7)$$

where q_{ii} are ingredients of the EFG tensor at the quadrupole nucleus determined in the EFG principal axes system, Q is the nuclear quadrupole moment, e is the proton charge and h is the Planck's constant [36, 37].

In this research work, the electric potential as the quantity of work energy through carrying over the electric charge from one position to another position in the essence of electric field has been evaluated for "CO@Ti–B_4N_{10}_NC, CO@V–B_4N_{10}_NC, CO@Cr–B_4N_{10}_NC, CO@Co–B_4N_{10}_NC, CO@Cu–B_4N_{10}_NC, and CO@Zn–B_4N_{10}_NC" complexes (Table 1 & Table 2).

Doping atoms of Ti(15), V(15), Cr(15), Co(15), Cu(15), Zn(15) on the B_5N_{10}_NC have shown the most potential for accepting the electron from the electron donor of C(1) and O(2) in CO adsorbed on the X–B_4N_{10}_NC (Figure 3).

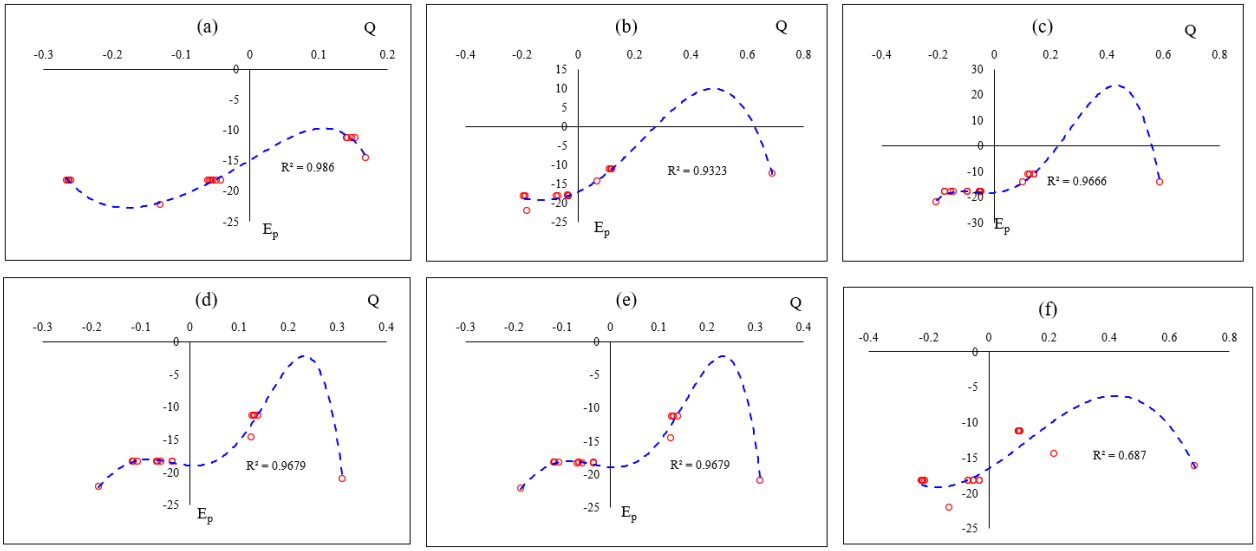

Figure 3 "Electric potential (a.u.) versus Bader charge (coulomb)" for **a)** CO@Ti–B_4N_{10}_NC, **b)** CO@V–B_4N_{10}_NC, **c)** CO@Cr–B_4N_{10}_NC, **d)** CO@Co–B_4N_{10}_NC, **e)** CO@Cu–B_4N_{10}_NC, and **f)** CO@Zn–B_4N_{10}_NC complexes.

In Figure 3(a) and (b), it was observed the behavior of CO adsorption on the Ti–B_4N_{10}_NC and CO@V–B_4N_{10}_NC, with the analogous high sensitivity based on the relation coefficient of R^2 = 0.986 and R^2 = 0.9323, respectively. Adsorption of CO on the Cr–B_4N_{10}_NC, Co–B_4N_{10}_NC and Cu–B_4N_{10}_NC in Figure 3(c), (d) and (e), respectively, has illustrated the highest sensing of R^2 = 0.9666, and R^2 = 0.9679 (both Co–B_4N_{10}_NC and Cu–B_4N_{10}_NC). However, Figure 3(f) has resulted that CO@Zn–B_4N_{10}_NC has a lower potential than other nanocage surfaces for CO removal from air (R^2 = 0.687). The adsorbents of chromium with 0.5883, zinc with 0.6853, vanadium with 0.6893, and titanium with 0.7499 coulomb, respectively, have presented the most tendency for being the electron acceptors. The uptake of gas molecules has been known to be associated with X–B_4N_{10}_NC, indicating that the adsorbed CO molecules in the X–X-doped nanocage can be internalized through a different pathway from pristine nanocage.

The chemical shielding resulted from NMR [38] spectroscopy including isotropic (σ_{iso}) and anisotropic (σ_{aniso}) for gas molecules trapped in the X–B_4N_{10}_NC towards the formation of CO@Ti–B_4N_{10}_NC, CO@V–B_4N_{10}_NC, CO@Cr–B_4N_{10}_NC, CO@Co–B_4N_{10}_NC, CO@Cu–B_4N_{10}_NC, and CO@Zn–B_4N_{10}_NC complexes have been computed by Gaussian 16 revision C.01 program package [30] and been shown in Table 3 & Table 4.

Table 3 NMR tensors (ppm) for selected atoms of CO@Ti–B_4N_{10}_NC, CO@V–B_4N_{10}_NC, CO@Cr–B_4N_{10}_NC, and CO@Co–B_4N_{10}_NC complexes.

CO@Ti–B_4N_{10}_NC			CO@V–B_4N_{10}_NC			CO@Cr–B_4N_{10}_NC		
Atom	σ_{iso}	σ_{aniso}	Atom	σ_{iso}	σ_{aniso}	Atom	σ_{iso}	σ_{aniso}
C1	388.8511	666.7627	C1	260.9712	393.3751	C1	292.1782	694.1805
O2	1283.8732	1685.3315	O2	735.9242	1104.0681	O2	633.1859	3188.7465
B3	117.2886	102.8982	B3	70.3244	66.7736	B3	39.2967	99.6046
N4	891.6795	12840.5030	N4	1177.9192	1203.5066	N4	1870.0279	2661.9993
N5	2581.3254	13809.2948	N5	819.5890	610.2603	N5	131.5764	2171.5379
B6	85.0063	73.4353	B6	70.5210	67.1702	B6	52.5392	46.2836
B7	113.4469	184.3166	B7	70.2874	67.7906	B7	38.0691	111.9754
B8	100.3561	104.0940	B8	70.3698	67.5527	B8	54.2128	45.9159
N9	2515.2774	4029.0751	N9	109.5248	931.7893	N9	378.9198	1752.4055
N10	1147.6386	15164.8980	N10	784.4759	495.8301	N10	928.6784	2162.4106
N11	1403.4501	2850.4956	N11	598.2535	722.0654	N11	813.3494	2124.0132
N12	1553.1439	3084.0244	N12	609.7100	892.8854	N12	70.9784	2292.9194
N13	848.1172	2567.4336	N13	560.6195	750.5350	N13	1115.8864	2122.6552
N14	706.4805	2271.1598	N14	540.1301	766.4368	N14	147.3939	1954.1015
Ti15	1187.2260	1138.4861	**V15**	4008.2481	478.9168	**Cr15**	12676.2274	4962.3842
N16	290.9426	5510.7548	N16	94.5760	753.2783	N16	14.0527	1720.0787
N17	3332.5747	7753.1427	N17	1248.6618	1250.0664	N17	1283.8952	4581.8198

Table 4 NMR tensors (ppm) for selected atoms of CO@Co–B_4N_{10}_NC, CO@Cu–B_4N_{10}_NC, and CO@Zn–B_4N_{10}_NC complexes.

CO@Co–B_4N_{10}_NC			CO@Cu–B_4N_{10}_NC			CO@Zn–B_4N_{10}_NC		
Atom	σ_{iso}	σ_{aniso}	Atom	σ_{iso}	σ_{aniso}	Atom	σ_{iso}	σ_{aniso}
C1	236.7354	564.5258	C1	203.5355	617.4635	C1	257.7474	592.4371
O2	734.6573	1565.6378	O2	726.2906	1300.8011	O2	843.7191	1329.2058
B3	68.9199	67.7533	B3	72.2837	77.4514	B3	97.6044	107.2476
N4	364.1386	807.7547	N4	595.1884	1409.1634	N4	2231.2755	5778.7287
N5	328.3577	1013.4882	N5	545.3801	617.9658	N5	476.9844	9155.3197
B6	57.9880	75.7327	B6	63.8370	79.6242	B6	87.7693	106.0778
B7	58.2838	70.2613	B7	63.7860	78.3922	B7	92.6279	113.0517
B8	70.0946	74.7531	B8	72.6591	78.0618	B8	89.0662	96.9983
N9	344.3997	658.6215	N9	338.7207	254.9285	N9	2048.7010	8332.6107
N10	384.4197	935.6162	N10	540.1666	624.4985	N10	379.2790	8951.7586
N11	911.7619	703.4108	N11	454.4266	357.8068	N11	785.1710	1756.5284
N12	792.8207	735.7745	N12	473.0107	371.9460	N12	513.8596	1121.0887
N13	781.2989	680.5794	N13	523.3912	680.3183	N13	1255.5158	1825.1782
N14	736.7560	539.9430	N14	532.5175	679.2489	N14	791.7575	1017.0261
Co15	12319.7965	4125.6887	**Cu15**	2243.5444	806.4926	**Zn15**	335.1748	1057.4872
N16	391.9645	522.6333	N16	246.6325	550.8873	N16	2106.9316	8278.3243
N17	359.8620	1190.9198	N17	428.7270	601.6366	N17	2872.1260	5426.2698

NMR parameter (ppm) has reported the notable amounts for CO which were adsorbed on the X–B_4N_{10}_NC (Table 3 & Table 4). The increase in the NMR anisotropy spans for C(1) and O(2) atoms of CO adsorption on the X–B_4N_{10}_NC. Notably, doping of Ti, V, Cr, Co, Cu, and Zn on B_4N_{10}_NC might promote the strength of nanocage. The adsorption of CO can present spin polarization on the X–B_4N_{10}_NC which indicates that these nano-surfaces may be employed as magnetic scavenging surfaces as a gas detector.

Figure 4(a-f) indicates the similar orientation of NMR parameter (ppm) for boron and nitrogen; however, a remarkable deviation is observed from doping atoms of Ti(15), V(15), Cr(15), Co(15), Cu(15), Zn(15) through interaction with C(1) and O(2) of CO during adsorbing on the B_5N_{10}_NC.

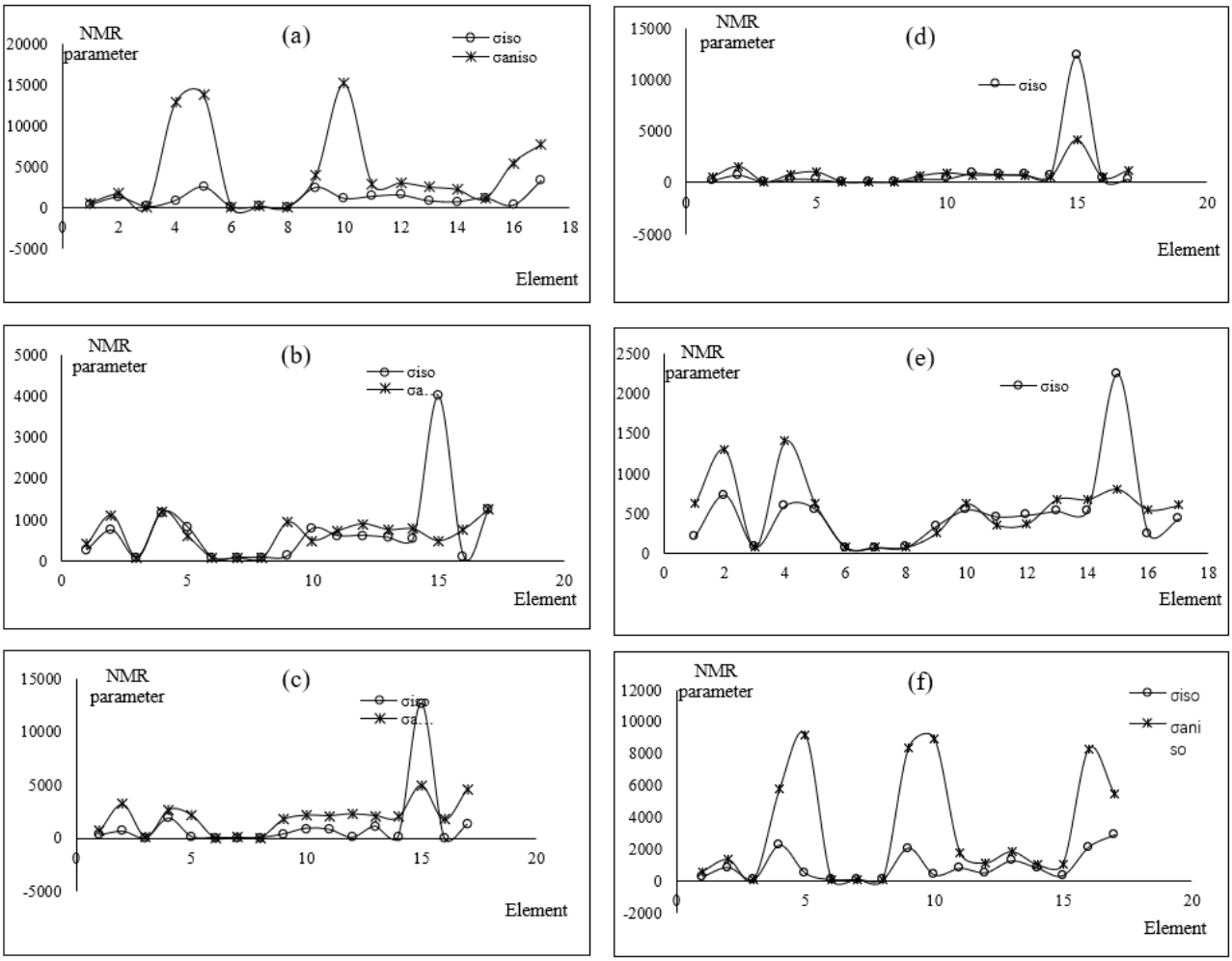

Figure 4 NMR tensors (ppm) for **a)** CO@Ti–B_4N_{10}_NC, **b)** CO@V–B_4N_{10}_NC, **c)** CO@Cr–B_4N_{10}_NC, **d)** CO@Co–B_4N_{10}_NC, **e)** CO@Cu–B_4N_{10}_NC, and **f)** CO@Zn–B_4N_{10}_NC complexes using CAM–B3LYP–D3/6-311+G (d,p), LANL2DZ.

In Figure 4(a-f), gas molecules of CO in the complexes of CO@Ti–B_4N_{10}_NC (Figure 4a), CO@V–B_4N_{10}_NC (Figure 4b), CO@Cr–B_4N_{10}_NC (Figure 4c), CO@Co–B_4N_{10}_NC (Figure 4d), CO@Cu–B_4N_{10}_NC (Figure 4e), and CO@Zn–B_4N_{10}_NC (Figure 4f) exhibit the alteration in the NMR parameter among gas grabbing.

The IR calculations have been done for the adsorption of CO molecules by X–B_4N_{10}_NC during toxic gas sensing in air. Therefore, it has been simulated the several clusters containing CO@Ti–B_4N_{10}_NC (Figure 5a), CO@V–B_4N_{10}_NC (Figure 5b), CO@Cr–B_4N_{10}_NC (Figure 5c), CO@Co–B_4N_{10}_NC (Figure 5d), CO@Cu–B_4N_{10}_NC (Figure 5e) and CO@Zn–B_4N_{10}_NC (Figure 5f) complexes.

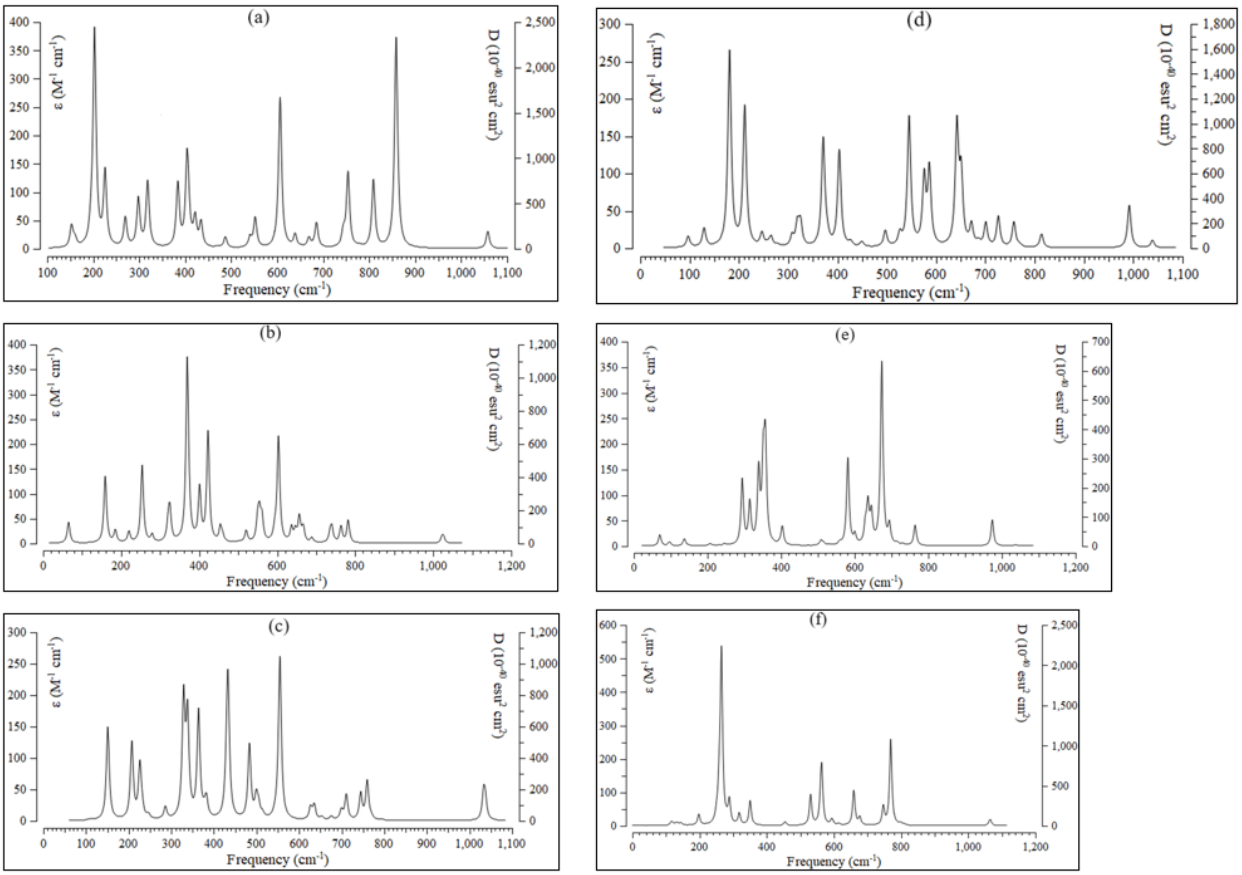

Figure 5 IR spectra for **a)** CO@Ti–B_4N_{10}_NC, **b)** CO@V–B_4N_{10}_NC, **c)** CO@Cr–B_4N_{10}_NC, **d)** CO@Co–B_4N_{10}_NC, **e)** CO@Cu–B_4N_{10}_NC, and **f)** CO@Zn–B_4N_{10}_NC complexes.

The graph of Figure 5(a) has been observed in the frequency range between 100–1100 cm^{-1} for CO@Ti–B_4N_{10}_NC with sharp peaks around 202.69, 606.23 and 858.53 cm^{-1}. Figure 5(b) has shown the frequency range between 100–1100 cm^{-1} for CO@V–B_4N_{10}_NC with two sharp peaks around 369.36, 422.65 and 603.26 cm^{-1}. Figure 5(c) has indicated the fluctuation of frequency between 100–1100 cm^{-1} for CO@Cr–B_4N_{10}_NC with several sharp peaks around 328.93, 433.18 and 554.91 cm^{-1}. Figure 5(d) has shown the fluctuation of frequency between 100–1100 cm^{-1} for CO@Co–B_4N_{10}_NC with sharp peaks around 180.91, 211.68, 370.94, 403.62, 545.15, and 642.16 cm^{-1}. Moreover, it has been observed that the frequency between 200–1100 for CO@Cu–B_4N_{10}_NC with sharp peaks around 357.09, 581.27 and 673.35 cm^{-1} (Figure 5e). Besides, Figure 5(f) has exhibited the frequency between 200–1100 for CO@Zn–B_4N_{10}_NC with sharp peaks around 264.84, 563.65 and 769.01cm^{-1}.

Thermodynamic specifications have been concluded that X–B_4N_{10}_NC due to adsorption of CO might be more efficient sensors for detecting and removing the gas molecules from the polluted air (Table 5).

Table 5 The thermodynamic characters of CO@Ti–B_4N_{10}_NC, CO@V–B_4N_{10}_NC, CO@Cr–B_4N_{10}_NC, CO@Co–B_4N_{10}_NC, CO@Cu–B_4N_{10}_NC, and CO@Zn–B_4N_{10}_NC complexes using CAM–B3LYP–D3/6–311+G (d,p), LANL2DZ calculation.

Compound	ΔE° × 10^{-3} (kcal/mol)	ΔH° × 10^{-3} (kcal/mol)	ΔG° × 10^{-3} (kcal/mol)	S° (cal/K.mol)	Dipole moment (Debye)
CO@Ti–B_4N_{10}_NC	-512.565	-512.564	-512.595	102.375	3.4889
CO@V–B_4N_{10}_NC	-521.152	-521.152	-521.183	106.021	1.1206
CO@Cr–B_4N_{10}_NC	-530.213	-530.213	-530.244	104.267	1.2359
CO@Co–B_4N_{10}_NC	-567.365	-567.365	-567.397	108.482	1.2664
CO@Cu–B_4N_{10}_NC	-599.390	-599.389	-599.422	109.196	1.5135
CO@Zn–B_4N_{10}_NC	-517.415	-517.415	-517.448	113.042	3.3803

It has been indicated that for a given number of carbon donor sites in CO, the stabilities of complexes owing to doping atoms of Ti, V, Cr, Co, Cu, Zn can be considered as: CO@Cu–B_4N_{10}_NC >> CO@Co–B_4N_{10}_NC > CO@Cr–B_4N_{10}_NC > CO@V–B_4N_{10}_NC > CO@Zn–B_4N_{10}_NC > CO@Ti–B_4N_{10}_NC (Table 5).

The adsorption process of CO gas molecules on the X–B_4N_{10}_NC is affirmed by the ΔG°_{ads} quantities:

$$\Delta G^{\circ}_{ads} = \Delta G^{\circ}_{CO@X\text{–}B_4N_{10}\_NC} - \left(\Delta G^{\circ}_{CO} + \Delta G^{\circ}_{X\text{–}B_4N_{10}\_NC}\right); \quad X=Ti, V, Cr, Co, Cu, Zn \qquad (8)$$

Figure 6 has shown that the key role of doped atoms of Ti, V, Cr, Co, Cu, Zn during interaction between the adsorbates of CO gas molecules as the electron donors and the adsorbent of Ti–B_4N_{10}_NC, V–B_4N_{10}_NC, Cr–B_4N_{10}_NC, Co–B_4N_{10}_NC, Cu–B_4N_{10}_NC, and Zn–B_4N_{10}_NC as electron acceptors. Therefore, the selectivity of atom-doped on boron nitride nanocage (gas sensor) for gas molecules adsorption can be resulted as: Cu >> Co > Cr > V > Zn > Ti (Table 5 & Figure 6).

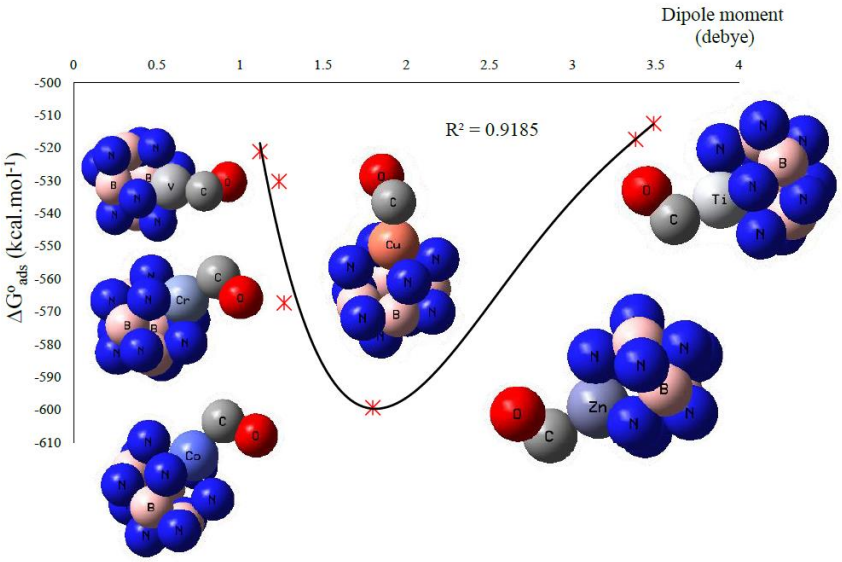

Figure 6 The Gibbs free energy (ΔG°_{ads}) versus dipole moment (Debye) for CO@Ti–B_4N_{10}_NC, CO@V–B_4N_{10}_NC, CO@Cr–B_4N_{10}_NC, CO@Co–B_4N_{10}_NC, CO@Cu–B_4N_{10}_NC, and CO@Zn–B_4N_{10}_NC complexes.

A strong donor–acceptor interaction between CO and TM–doped B_4N_{10}_NC has been probed. The orbital distribution analysis shows that electrons are delocalized around the adsorption site. Energy gaps and density of states of TM–doped B_4N_{10}_NC are significantly changed after CO adsorption, corresponding to the significant change of electrical conductivity of TM–doped BNNSs. In conclusion, TM–doped B_4N_{10}_NC are strongly reactive and sensitive to CO molecule and therefore it can be used as adsorption and sensing nanomaterials.

4. Conclusion

Various industries utilize gas sensors for environmental monitoring. The advantage of the gas sensors is limited due to the low sensitivity of sensing nanomaterial produced from pristine structures. The functionalization of pristine nanomaterial leads to enhanced adsorption reactivity and improvement of sensitivity. Many theoretical studies suggest that the functionalization by impurity atom doping in nanomaterial can enhance chemical reactivity. This research has investigated the doping of Ti, V, Cr, Co, Cu, and Zn transition metals in the boron nitride nanocage (X–B_4N_{10}_NC) for enhancing toxic gas sensing of these nanomaterials in air pollution removal. Therefore, CO gas molecule separation involving X–B_4N_{10}_NC has been experimentally investigated based on electrostatic interactions between the gas molecules and X–B_4N_{10}_NC. The electromagnetic and thermodynamic properties of X–B_4N_{10}_NC complexes were computed using the DFT method. The data has demonstrated that the chosen gas molecules adsorbed on the X–B_4N_{10}_NC are relatively stable, with the most stable adsorption site being in the center of the X–B_4N_{10}_NC system. The selectivity of atom-doped on boron nitride nanocages (gas sensor) for gas molecule adsorption can be as follows: CO@Cu–B_4N_{10}_NC > CO@Co–B_4N_{10}_NC > CO@Cr–B_4N_{10}_NC > CO@V–B_4N_{10}_NC > CO@Zn–B_4N_{10}_NC > CO@Ti–B_4N_{10}_NC, respectively.

Acknowledgments

The author is grateful to Kastamonu University for completing this paper and its research.

Author Contributions

Fatemeh Mollaamin (F.M.): Conceptualization, writing – original draft, formal analysis, writing – review and editing. The author has read and approved the published version of the manuscript.

Competing Interests

The authors have declared that no competing interests exist. The author states the topic selection, innovations and methods, etc. of this study are not duplicated in authors' published articles.

References

1. Gonzalez-Ortiz D, Salameh C, Bechelany M, Miele P. Nanostructured boron nitride–based materials: Synthesis and applications. Mater Today Adv. 2020; 8: 100107.
2. Mishra NS, Saravanan P. A review on the synergistic features of hexagonal boron nitride (white graphene) as adsorbent-photo active nanomaterial. ChemistrySelect. 2018; 3: 8023-8034.

3. Weng Q, Wang X, Wang X, Bando Y, Golberg D. Functionalized hexagonal boron nitride nanomaterials: Emerging properties and applications. Chem Soc Rev. 2016; 45: 3989-4012.
4. Muñoz AD, Escobedo-Morales A, Skakerzadeh E, Anota EC. Effect of homonuclear boron bonds in the adsorption of DNA nucleobases on boron nitride nanosheets. J Mol Liq. 2021; 322: 114951.
5. Shtansky DV, Matveev AT, Permyakova ES, Leybo DV, Konopatsky AS, Sorokin PB. Recent progress in fabrication and application of BN nanostructures and BN-based nanohybrids. Nanomaterials. 2022; 12: 2810.
6. Yang Y, Peng Y, Saleem MF, Chen Z, Sun W. Hexagonal boron nitride on III-V compounds: A review of the synthesis and applications. Materials. 2022; 15: 4396.
7. Davies A, Albar JD, Summerfield A, Thomas JC, Cheng TS, Korolkov VV, et al. Lattice-matched epitaxial graphene grown on boron nitride. Nano Lett. 2018; 18: 498-504.
8. Bangari RS, Yadav VK, Singh JK, Sinha N. Fe_3O_4-Functionalized boron nitride nanosheets as novel adsorbents for removal of arsenic (III) from contaminated water. ACS Omega. 2020; 5: 10301-10314.
9. Chao Y, Zhang J, Li H, Wu P, Li X, Chang H, et al. Synthesis of boron nitride nanosheets with N-defects for efficient tetracycline antibiotics adsorptive removal. Chem Eng J. 2020; 387: 124138.
10. Vatanpour V, Naziri Mehrabani SA, Keskin B, Arabi N, Zeytuncu B, Koyuncu I. A comprehensive review on the applications of boron nitride nanomaterials in membrane fabrication and modification. Ind Eng Chem Res. 2021; 60: 13391-13424.
11. Larki S, Shakerzadeh E, Anota EC, Behjatmanesh-Ardakani R. The Al, Ga and Sc dopants effect on the adsorption performance of $B_{12}N_{12}$ nanocluster toward pnictogen hydrides. Chem Phys. 2019; 526: 110424.
12. Guo Y, Wang R, Wang P, Rao L, Wang C. Developing a novel layered boron nitride–carbon nitride composite with high efficiency and selectivity to remove protonated dyes from water. ACS Sustain Chem Eng. 2019; 7: 5727-5741.
13. Carrillo I, Ramírez JM, Magaña LF. Adsorption of carbon monoxide, carbon dioxide and methane on hexagonal boron nitride with high titanium coverage. Surf Sci. 2015; 637: 48-52.
14. Tabtimsai C, Rakrai W, Kaewtong C, Wanno B. CO gas adsorption and detection ability of boron nitride nanosheet doping with group 8B transition metal: A theoretical investigation. Diam Relat Mater. 2023; 133: 109694.
15. Silva AL, de Jesus Gomes Varela Júnior J. Carbon monoxide interaction with $B_{12}N_{12}$ nanocage with and without an external electric field: A DFT study. J Nanoparticle Res. 2022; 24: 1.
16. Ammar HY, Badran HM, Eid KM. TM-doped $B_{12}N_{12}$ nano-cage (TM = Mn, Fe) as a sensor for CO, NO, and NH_3 gases: A DFT and TD-DFT study. Mater Today Commun. 2020; 25: 101681.
17. Henkelman G, Arnaldsson A, Jónsson H. A fast and robust algorithm for Bader decomposition of charge density. Comput Mater Sci. 2006; 36: 354-360.
18. Blöchl PE. Projector augmented-wave method. Phys Rev B. 1994; 50: 17953-17979.
19. Perdew JP, Burke K, Ernzerhof M. Generalized gradient approximation made simple. Phys Rev Lett. 1996; 77: 3865.
20. Ziesche P, Kurth S, Perdew JP. Density functionals from LDA to GGA. Comput Mater Sci. 1998; 11: 122-127.

21. Arrigoni M, Madsen GK. Comparing the performance of LDA and GGA functionals in predicting the lattice thermal conductivity of III-V semiconductor materials in the zincblende structure: The cases of AlAs and BAs. Comput Mater Sci. 2019; 156: 354-360.
22. Hohenberg P, Kohn W. Inhomogeneous electron gas. Phys Rev. 1964; 136: B864-B871.
23. Kohn W, Sham LJ. Self-consistent equations including exchange and correlation effects. Phys Rev. 1965; 140: A1133-A1138.
24. Becke AD. Density-functional thermochemistry. III. The role of exact exchange. J Chem Phys. 1993; 98: 5648-5652.
25. Lee C, Yang W, Parr RG. Development of the Colle-Salvetti correlation-energy formula into a functional of the electron density. Phys Rev B. 1988; 37: 785-789.
26. Kim K, Jordan KD. Comparison of density functional and MP2 calculations on the water monomer and dimer. J Phys Chem. 1994; 98: 10089-10094.
27. Stephens PJ, Devlin FJ, Chabalowski CF, Frisch MJ. Ab initio calculation of vibrational absorption and circular dichroism spectra using density functional force fields. J Phys Chem. 1994; 98: 11623-11627.
28. Cramer CJ. Essentials of computational chemistry: Theories and models. 2nd ed. John Wiley & Sons; 2004.
29. Mollaamin F, Monajjemi M. Corrosion inhibiting by some organic heterocyclic inhibitors through Langmuir adsorption mechanism on the Al-X (X = Mg/Ga/Si) alloy surface: A study of quantum three-layer method of CAM-DFT/ONIOM. Journal of Bio Tribo Corros. 2023; 9: 33.
30. Mollaamin F, Monajjemi M. Molecular modelling framework of metal-organic clusters for conserving surfaces: Langmuir sorption through the TD-DFT/ONIOM approach. Mol Simul. 2023; 49: 365-376.
31. Vosko SH, Wilk L, Nusair M. Accurate spin-dependent electron liquid correlation energies for local spin density calculations: A critical analysis. Can J Phys. 1980; 58: 1200-1211.
32. Frisch ME, Trucks GW, Schlegel HB, Scuseria GE, Robb M, Cheeseman JR, et al. Gaussian 16. Revision C.01. Wallingford, CT: Gaussian, Inc.; 2016.
33. Dennington RD, Keith TA, Millam JM. GaussView, version 6.06.16. Shawnee Mission, KS: Semichem Inc.; 2016.
34. Smith JA. Nuclear quadrupole resonance spectroscopy. General principles. J Chem Educ. 1971; 48: 39-41.
35. Garroway AN. Appendix K: Nuclear quadrupole resonance. Alternatives for Landmine Detection. Santa Monica, CA: Rand Corporation; 2003; Report MR-1608.
36. Poleshchuk OK, Kalinina EL, Latosińska JN, Koput J. Application of density functional theory to the analysis of electronic structure and quadrupole interaction in dimers of transition and non-transition elements. J Mol Struct Theochem. 2001; 574: 233-243.
37. Young HD, Freedman RA. Sears and Zemansky's University Physics with Modern Physics. 13th ed. Boston, MA: Addison-Wesley; 2012.
38. Sohail U, Ullah F, Binti Zainal Arfan NH, Abdul Hamid MH, Mahmood T, Sheikh NS, et al. Transition metal sensing with nitrogenated holey graphene: A first-principles investigation. Molecules. 2023; 28: 4060.